



Underlying Mechanisms of Crack Initiation for Granitic Rocks Containing a Single Pre-existing Flaw: Insights From Digital Image Correlation (DIC) Analysis

Liwang Liu^{1,2} · Haibo Li^{1,2} · Xiaofeng Li¹ · Di Wu^{1,2} · Guokai Zhang³

Received: 2 December 2019 / Accepted: 21 October 2020 / Published online: 20 November 2020
© Springer-Verlag GmbH Austria, part of Springer Nature 2020

Abstract

Determination on underlying mechanisms of crack initiation is of vital importance to understand the failure processes of geo-materials in practical engineering. In this study, uniaxial compression experiments of granitic samples containing a single pre-existing flaw were conducted and the failure processes were recorded by using the high-speed camera. To quantitatively determine the crack initiation mechanism, a novel method was first proposed based on digital image correlation (DIC) analysis and then its validity was confirmed. By utilizing this method, three types of cracks with different initiation mechanisms were identified and the effect of flaw inclination angle on crack initiation mechanisms was discussed from the viewpoint of theoretical analysis. With the increase of inclination angles, wing cracks change from mixed mode I/II cracks to mode I cracks, while anti-wing cracks have no evident changes and are dominated by mode II cracks. Under compressive pressure, the upper and bottom surfaces of pre-existing flaw deform to each other and the distributions of full-field tangential stress around flaw are different, which might induce the variation of crack initiation mechanisms with regard to the inclination angle.

Keywords Crack initiation mechanisms · Digital image correlation (DIC) analysis · Wing cracks · Anti-wing cracks · Pre-existing flaw

1 Introduction

The failure of brittle materials which is associated with crack growth of intrinsic flaws commonly exists in the field of rock mechanics and engineering geology. From a large number of laboratory experimental results, the flaw existing in rock samples initiates and propagates at microscopic scale when subjected to external loading, which would induce the occurrence of some macroscopic phenomena, e.g., crack branching, volumetric dilation and brittle–ductile transition (Bieniawski 1967a, b; Nemat-Nasser et al. 1982; Horii and

Nemat-Nasser 1985; Martin and Chandler 1994; Li et al. 2018a, b, 2019). In addition, many disasters were encountered in engineering geology, including the failure of pillar in mines (Esterhuizen et al. 2011), the stability of rock slope (Brideau et al. 2009) and fault reactivation (Sibson 1985; Petit and Barquins 1988), which had intimate connection with the crack growth of flaws. Therefore, conducting investigation on initiation mechanisms of cracks emanating from flaws in rock materials is of significance to understand the failure processes.

During the last few decades, many experimental studies have been conducted to investigate cracking characteristics of rock materials. By utilizing conventional strain gauges, the characteristics of stress–strain curves were obtained and the failure process of intact rocks under compression was divided into five stages, which represented different states of crack growth (Bieniawski 1967a, b; Eberhardt et al. 1998). Since flaws existing in rocks have different length, inclination angles and distributions, thus above five stages obtained from experiments of intact samples are rather difficult to reveal the detailed initiation and propagation processes of a single flaw. To overcome these problems, samples

✉ Xiaofeng Li
xfli@whrsm.ac.cn

¹ State Key Laboratory of Geomechanics and Geotechnical Engineering, Institute of Rock and Soil Mechanics, Chinese Academy of Sciences, Wuhan 430071, China

² University of Chinese Academy of Sciences, Beijing 100049, China

³ School of Mechanical Engineering, Nanjing University of Science and Technology, Nanjing, 210094, China

containing pre-existing flaws were artificially fabricated and numerous experiments were conducted to investigate the cracking characteristics of rock and rock-like materials (Bobet and Einstein 1998; Wong and Chau 1998; Sagong and Bobet 2002; Wong et al. 2004; Li et al. 2005; Wong and Einstein 2006; Yang et al. 2008, 2013). In the early period, due to the limitation of measurement technique, crack initiation patterns were determined based on the observation of stress-induced crack surface. When the crack surface is clean or accompanied with a plumose structure, the crack type is classified as tensile crack. If the surface is rough or covered by pulverized powder, the crack type is defined as shear crack (Shen et al. 1995; Bobet and Einstein 1998; Wong and Einstein 2006, 2009a; Park and Bobet 2009; Lee and Jeon 2011). Subsequently, in cooperation with high-speed camera, images illustrating the failure processes of samples could be captured and Wong and Einstein (2009b) identified seven different crack types in marble samples containing a single flaw, including three types of tensile cracks, three types of shear cracks and one type of mixed tensile-shear crack. Whereas, Yang and Jing (2011) determined nine crack types in sandstone samples containing a single flaw by using the same method. Though the slight discrepancy of cracks emanating from flaws could be obtained by comparing two adjacent images, the method for determining crack initiation mechanisms was subjective, which might be the reason why above experimental results concerning crack initiation types were not consistent. In the ideal sliding crack model developed by Nemat-Nasser et al. (1982) and Horii and Nemat-Nasser (1985), the upper and bottom surfaces of pre-existing flaws were in touch and slip against each other, inducing that the tensile stress appeared around flaw tips and wing cracks consequently initiated as tensile cracks. In comparison, the flaws prefabricated in experiments of rock or rock-like materials are not ideal and the crack surfaces may not be adequately close under uniaxial compression (Bombolakis 1968; Li et al. 2020), revealing the initiation mechanisms of cracks emanating from pre-existing flaws in experiments are rather complicated.

To quantitatively investigate the crack initiation mechanisms in samples containing pre-existing flaws, the acoustic emission (AE) method with the ability of detecting and capturing the elastic wave induced by crack initiation (Rice 1980) has been extensively utilized. Based on the theory of AE source location and moment tensor inversion, the position of stress-induced microcracks could be determined (Lockner et al. 1991; Reches and Lockner 1994) and cracks initiated by different fracture mechanisms could be classified into tensile cracks, shear cracks and mixed mode cracks (Ohtsu 1991, 1995; Ohno and Ohtsu 2010). With the help of AE technique, the fracture processes of Carrara marble specimens containing a single pre-existing flaw were investigated, and three types of cracks were located and identified

during the experiments (Wong and Xiong 2018). However, the fracture mechanisms of above three types of cracks are still ambiguous, because the calculation principles of AE moment inversion are subjective and inaccurate. Recently, a new testing method, namely digital image correlation (DIC) analysis, has been developed and utilized in the field of solid mechanics (Chu et al. 1985; Xing et al. 2017; Ju et al. 2019a, b). Based on its merits of full-field and high accuracy, the method can be utilized to efficiently characterize the crack propagation processes (Guy et al. 2018). Zhao et al. (2018, 2019) investigated the fracture processes of rock-like samples containing one and two pre-existing flaws, the detailed processes of cracks initiation, propagation and coalescence were obtained. By analyzing the maximum principle strain and shear strain around flaw tips, Zhou et al. (2019) pointed out that the wing cracks initiated from flaw tips in experiments could be regarded as mixed tensile–shear cracks. Accordingly, it is efficient to investigate the crack initiation mechanism of granitic rocks containing a single pre-existing flaw by using DIC analysis.

In this study, granitic samples containing a single pre-existing flaw with different inclination angles were uniaxially compressed to failure. Based on digital image correlation analysis, a quantitative method for determining the underlying mechanisms of crack initiation in rock materials was first proposed and validated. Then, the crack types in samples containing flaws with different inclination angles were determined by using this quantitative method. To reveal the interpretation for the effect of inclination angle on the underlying crack initiation mechanism, the theoretical full-field tangential stress in samples with different inclination angles was analyzed and discussed in comparison with experimental results.

2 Experimental Methodology

2.1 Experimental Setup

As shown in Fig. 1a, the rock mechanics testing system consists of a loading apparatus (MTS 815.04) and a high-speed photographic system, the photographic system includes high-speed camera, light source and image acquisition systems, and the high-speed camera is a charge-coupled device (CCD) with resolution of 1624×1236 pixels. Before experiments, two ends of samples were treated with petroleum jelly to eliminate end friction effect and the high-speed photographic system was configured in front of samples with the optical axis of CCD perpendicular to the sample surface. At the beginning of experiments, the two systems were triggered simultaneously to record mechanical properties and fracture processes in real time. During the uniaxial compression, each sample was compressed at a slow loading

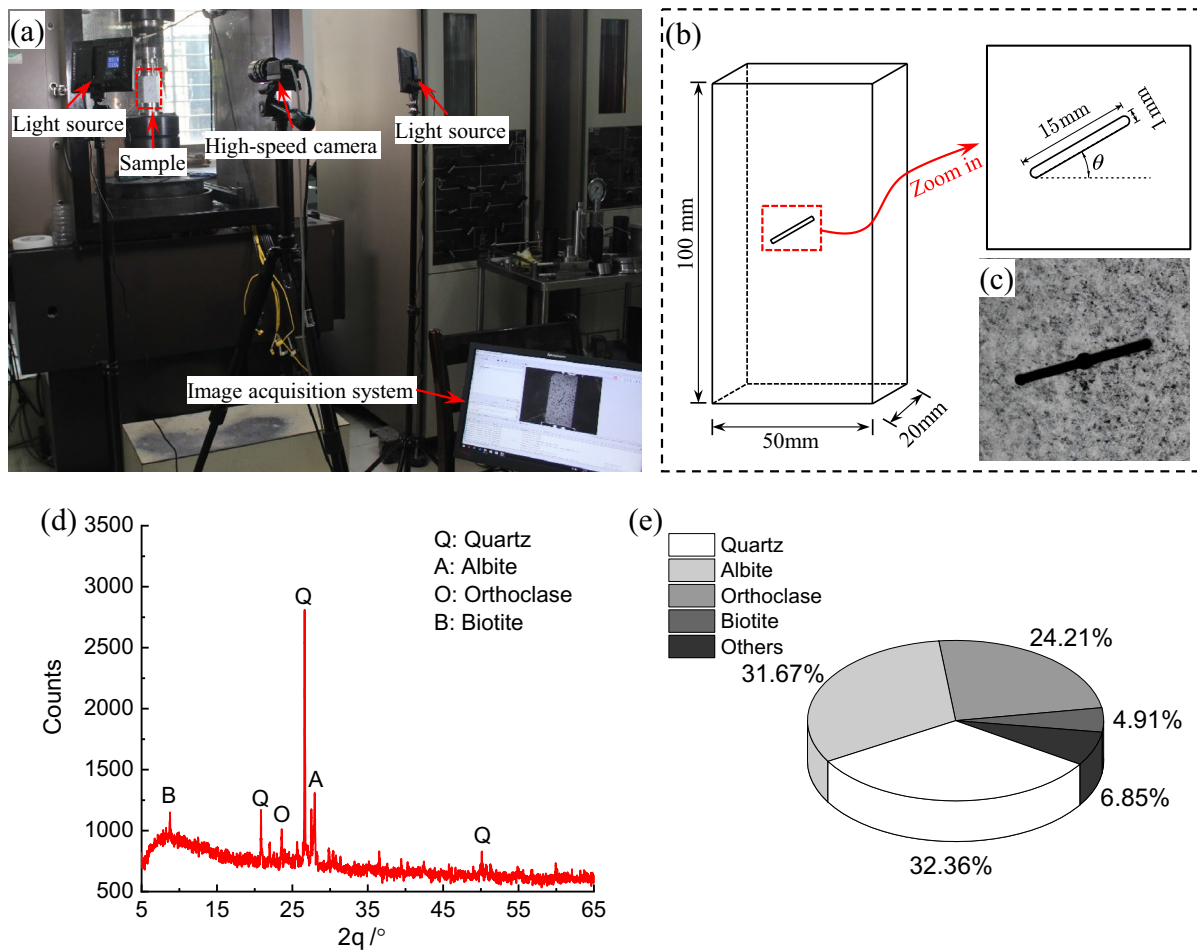


Fig. 1 Experimental apparatus and samples; **a** experimental apparatus; **b** sample geometry and pre-existing flaw size; **c** pre-existing flaw fabricated by water-jet machine in 15° sample; **d** results of XRD analysis; **e** proportion of mineral components

velocity along axial direction (0.0005 mm/s) to ensure the sample was in quasi-static condition. In addition, the sample rate of camera was set as 50 frames per second to capture the deformational images of sample surface for following DIC analysis.

2.2 Sample Preparation

The granitic samples were selected to investigate initiation mechanisms of cracks emanating from pre-existing flaws. According to experimental results of XRD analysis, the mineral components in granitic samples include quartz (32.36%), albite (31.67%), orthoclase (24.21%), biotite (4.91%) and others (6.85%). The compressive strength and tensile strength of samples are 236 MPa and 14.8 MPa, respectively. Referring to the previous literatures (Bobet and Einstein 1998; Li et al. 2005; Wong and Einstein 2009a, b; Lee and Jeon 2011), the samples in this study were designed as prismatic shape for better investigating the fracture processes. As presented in Fig. 1b, the dimension of samples is 50 mm in length,

20 mm in thickness and 100 mm in height. The pre-existing flaws with different inclination angles (θ varies from 0° to 90° with the increment of 15°) were prepared by utilizing water-jet machine, and the length and width of flaws are 15 mm and 1 mm, respectively.

Before testing, the random distributed speckles were applied on the surface of samples to meet the requirements of DIC analysis (Pan et al. 2009). As illustrated in Fig. 2a, the white paint was first uniformly sprayed on the sample surface after the surface had been cleaned. Then, the black paint was randomly covered over the white paint to obtain the speckles. According to the mean intensity gradient (denoted by δ_f) (Pan et al. 2010), the quality of speckle pattern after treatment is better than that before treatment.

2.3 Digital Image Correlation (DIC) Analysis

After capturing the sample images during uniaxial compression, the displacement and strain of sample surfaces can be calculated based on the analysis of digital image correlation

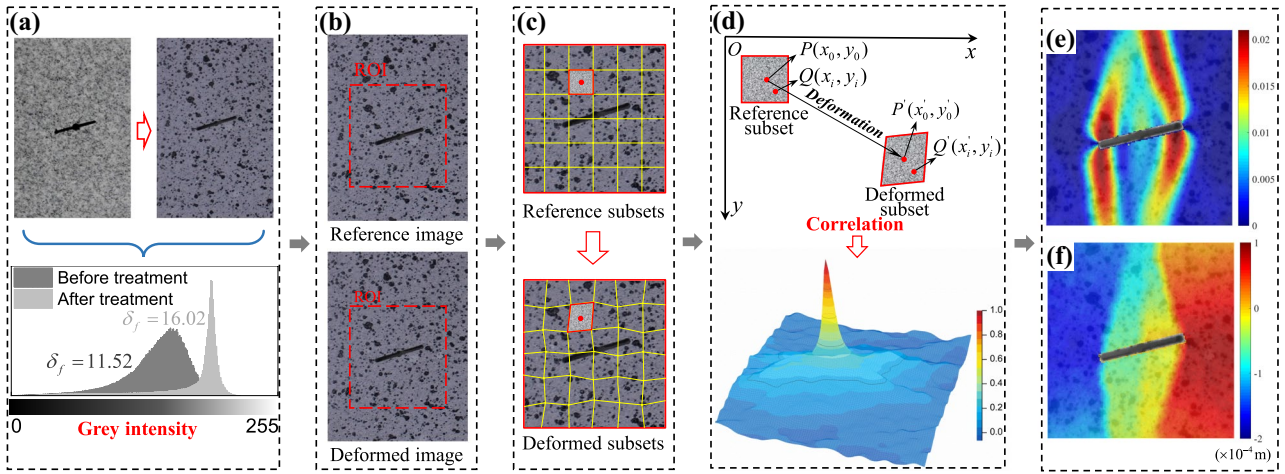


Fig. 2 The process of sample preparation and the flow chart for DIC calculation; **a** the treatment of sample surface for obtaining random distributed speckles; **b** ROI selection for analysis; **c** division of subset

into small subsets; **d** the principles of DIC analysis (modified after Pan et al. 2009); **e** strain field ϵ_{xx} when sample fails; **f** displacement u_{xx} field when sample fails

(DIC). As shown in Fig. 2b, the region of interest (ROI) was selected and then partitioned into many small subsets (Fig. 2c). When the sample surface deforms, the same subset in reference image and deformed image can be correlated based on the normalized cross-correlation (NCC) criteria (Blaber et al. 2015). The displacement components after deformation (Fig. 2f) are obtained by

$$x'_i - x_i = u_0 + \frac{\partial u}{\partial x}(x_i - x_0) + \frac{\partial u}{\partial y}(y_i - y_0), \quad (1)$$

$$y'_i - y_i = v_0 + \frac{\partial v}{\partial x}(x_i - x_0) + \frac{\partial v}{\partial y}(y_i - y_0), \quad (2)$$

where x_i , y_i , x'_i and y'_i are the coordinate component of points shown in Fig. 2d; u_0 and v_0 are the displacement component of the reference subset center in x and y directions; $\frac{\partial u}{\partial x}$, $\frac{\partial u}{\partial y}$, $\frac{\partial v}{\partial x}$ and $\frac{\partial v}{\partial y}$ are the first-order displacement gradient of the reference subset.

The strain components (Fig. 2e) in x and y directions can be calculated by

$$\epsilon_{xx} = \frac{1}{2} \left[2 \frac{\partial u}{\partial x} + \left(\frac{\partial u}{\partial x} \right)^2 + \left(\frac{\partial v}{\partial x} \right)^2 \right], \quad (3)$$

$$\epsilon_{yy} = \frac{1}{2} \left[2 \frac{\partial v}{\partial y} + \left(\frac{\partial u}{\partial y} \right)^2 + \left(\frac{\partial v}{\partial y} \right)^2 \right], \quad (4)$$

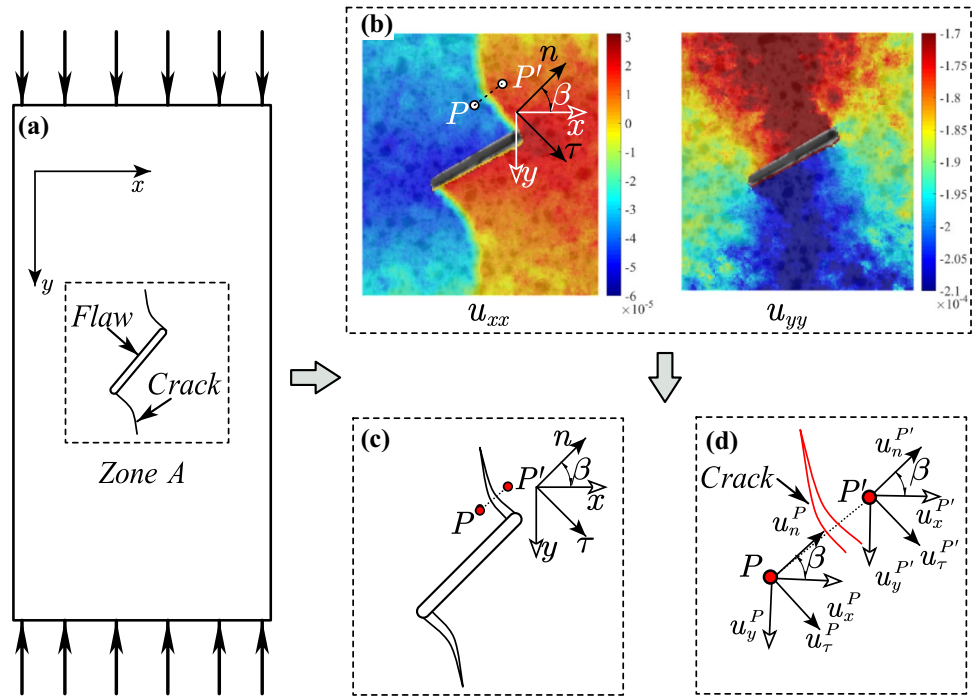
where ϵ_{xx} and ϵ_{yy} are the strain components of subset in x and y directions.

3 Method Description and Validation

3.1 Method Description

Due to the existence of stress concentration, cracks would initiate from the pre-existing flaw and the displacement components between them are different (Fig. 3a, b). In the previous literatures, the strain gauges were attached on the sample surface before experiments to study the fracture processes (Zhao et al. 2016; Yang et al. 2019). However, this method is rather complicated for experiment preparation and it is difficult to determine the locations for attaching strain gauges before experiments, because of the uncertainty of crack initiation positions and angles. In comparison, the digital image correlation (DIC) analysis has the ability to overcome above problems. As shown in Fig. 3b, to quantitatively evaluate the discrepancy of displacement components, two deformational monitoring points (i.e., points P and P') are first configured on the two sides of cracks and the line PP' is almost perpendicular to the crack initiation direction. Then, the displacement component of deformational monitoring points could be obtained in global coordinate, the displacement component of point P and P' are denoted by u_{xx}^P , u_{yy}^P and $u_{xx}^{P'}$, $u_{yy}^{P'}$, respectively (Fig. 3d). According to the displacement contours around flaw, the crack initiation position and initiation angle can be determined. As illustrated in Fig. 3c, the axis n represents the crack normal direction, the axis τ representing crack shear direction is perpendicular to the normal direction. The symbol β represents the angle between n axis and x axis, which can be used to transform

Fig. 3 The method for quantitatively determining crack initiation mechanisms; **a** schematic plot of initiated cracks under uniaxial compression; **b** full-field displacement components (u_{xx} and u_{yy}) of 15° sample surfaces in zone A; **c** schematic of displacement transformation from global coordinate to local coordinate (x and y represent global coordinate, n and τ represent local coordinate); **d** detailed displacement transformation of deformation monitoring points P and P'



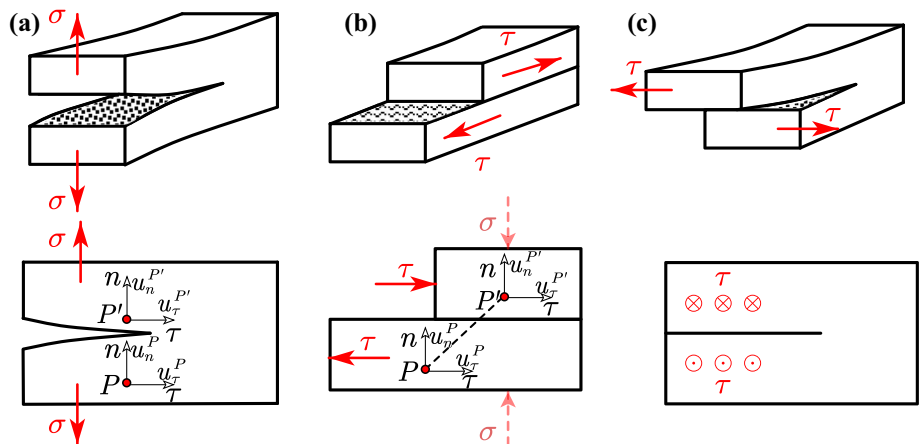
displacement components from global coordinate to local coordinate. The corresponding normal and shear displacement component of points P and P' in local coordinate are transformed by

$$\begin{bmatrix} u_n^P \\ u_\tau^P \end{bmatrix} = \begin{bmatrix} \cos \beta & -\sin \beta \\ \sin \beta & \cos \beta \end{bmatrix} \begin{bmatrix} u_x^P \\ u_y^P \end{bmatrix}, \tag{5}$$

$$\begin{bmatrix} u_n^{P'} \\ u_\tau^{P'} \end{bmatrix} = \begin{bmatrix} \cos \beta & -\sin \beta \\ \sin \beta & \cos \beta \end{bmatrix} \begin{bmatrix} u_x^{P'} \\ u_y^{P'} \end{bmatrix}, \tag{6}$$

where u_n^P , $u_n^{P'}$, u_τ^P and $u_\tau^{P'}$ are displacement components of points P and P' along the crack normal and shear directions, respectively.

Fig. 4 Three basic crack deformation modes in LEFM theory; **a** mode I (opening mode); **b** mode II (sliding mode); **c** mode III (tearing mode)



Then, the relative displacement component of points between two sides of the cracks can be obtained as

$$\Delta u_n = u_n^{P'} - u_n^P, \tag{7}$$

$$\Delta u_\tau = \left| u_\tau^{P'} - u_\tau^P \right|, \tag{8}$$

where Δu_n and Δu_τ are the normal and shear relative displacement of point P' with respect to point P .

Based on the assumption in linear elastic fracture mechanics (LEFM), the properties of cracks initiated under complex stress states can be investigated by the superposition of three basic crack tip deformation modes (Irwin 1957; Scavia 1995), which include mode I (opening mode), mode II (sliding mode) and mode III (tearing mode), as shown in Fig. 4. Since it is not easy to characterize the formation of mode III crack by DIC analysis, this type of crack is not taken into consideration in this study. As presented in Fig. 4a, when the tensile stress perpendicular to the surface of cracks overcomes material strength, the mode I cracks are generated. The upper and bottom surfaces of cracks would open, which indicates that the normal relative displacement is larger than 0, while the shear relative displacement has no obvious changes. Therefore, if the crack is mode I crack, the relative displacement component between points P and P' have to meet the following relationship:

$$\text{Mode I: } \left\{ u_n^{P'} - u_n^P > 0 \cup \left| u_\tau^{P'} - u_\tau^P \right| = 0 \right\}. \tag{9}$$

When the normal stress applied on the surface of crack is 0 or compressive stress, the two surfaces would keep touching

during the formation processes of cracks (Fig. 4b), revealing that the normal relative displacement is less than or equal to 0. In the meanwhile, the shear stress would induce the sliding of crack upper and bottom surfaces, so the shear relative displacement is larger than 0. As a consequence, if the crack is mode II crack, the relative displacement component between points P and P' have to meet the following relationship:

$$\text{Mode II: } \left\{ \left| u_\tau^{P'} - u_\tau^P \right| > 0 \cup u_n^{P'} - u_n^P \leq 0 \right\}. \tag{10}$$

Based on the aforementioned formulas (9) and (10), the basic crack modes (i.e., mode I and mode II cracks) can be quantitatively characterized using DIC analysis. When cracks form under complex stress state, the corresponding crack modes can be determined by the combination of above cracks.

3.2 Method Validation

Before using this method to determine initiation mechanisms of cracks in samples containing a single pre-existing flaw, it is necessary to confirm the method validity. According to the analysis conducted by Zhang and Wong (2012) and Wong and Einstein (2006) and the theory of open Griffith crack (Lajtai 1971), the pre-existing flaw fabricated in rock materials can be ideally considered as elliptical crack, the tangential stress around the crack boundary under uniaxial compression could be formularized as follows:

$$\sigma_{\beta\beta} = \sigma_0 \frac{\sinh 2\xi + e^{2\xi} \cos 2(\theta - \beta) - \cos 2\theta}{\cosh 2\xi - \cos 2\beta}, \tag{11}$$

where $\sigma_{\beta\beta}$ is the tangential stress around the boundary of Griffith crack, σ_0 is the applied compressive stress, ξ is a

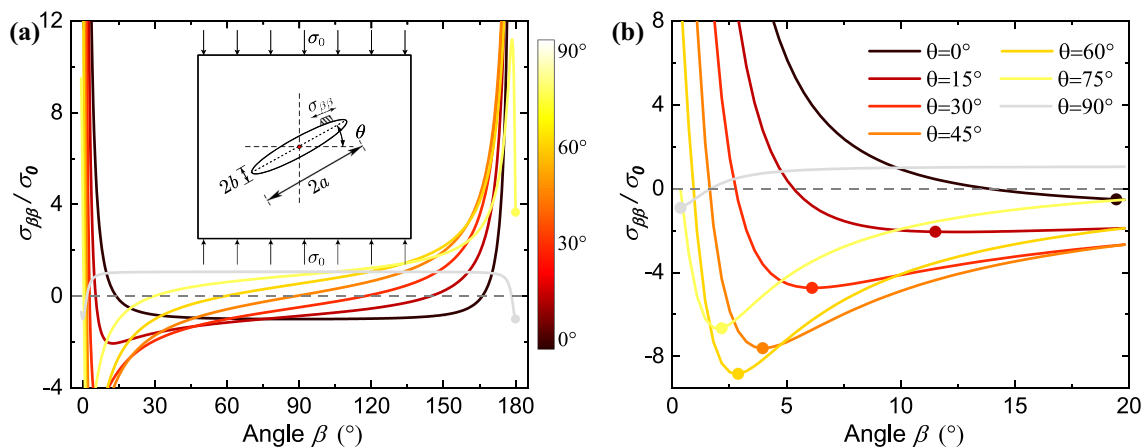


Fig. 5 Tangential stress around the boundary of Griffith crack; **a** tangential stress around the boundary of cracks with different inclination angle θ ; **b** the zoom-in view of tangential stress in zone A (the dots represent the maximum tensile tangential stress)

parameter in elliptical coordinate, ξ_0 is a constant that represents the crack boundary, β is the counter-clockwise angle of point on the crack boundary with respect to the direction of crack long axis, θ is the inclination angle of crack long axis (Fig. 5a).

Since the tensile strength of rock material is thought to be lower than its compressive strength, the stress-induced cracks are more likely to initiate from the place where the maximum tensile tangential stress is located. From Fig. 5a, the tangential stress around the crack boundary are complicated and have different changing tendencies with respect to inclination angles. Apparently, the possible crack initiation position where the tensile tangential stress is maximum moves from flaw tips to flaw center as the inclination angle θ decreases (Fig. 5b), which is concurrent with the results obtained by Wong and Einstein (2006).

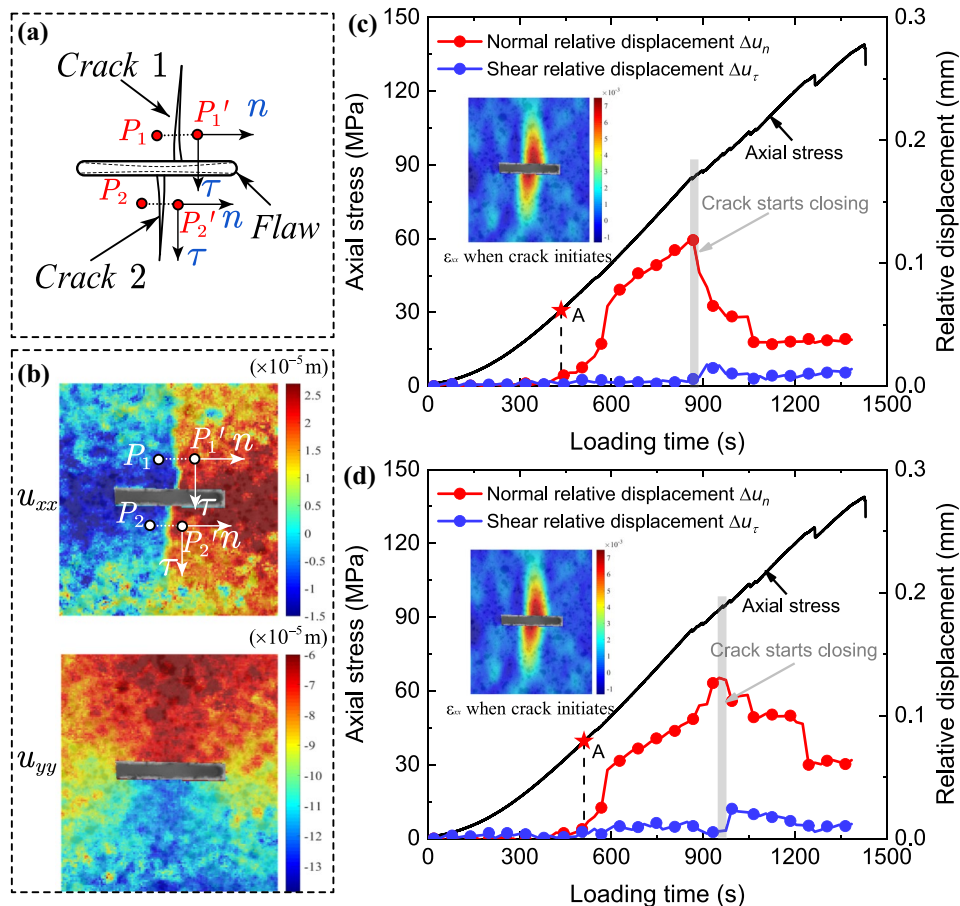
Despite the crack initiation location is easy to be derived via theoretical analysis, it is hard to guarantee the initiation positions in experiments agree well with the theoretical results except for 0° sample and 90° sample. For 0° sample, the crack initiation position obtained by theoretical analysis has wide extent ($\beta = 15^\circ - 165^\circ$). If the crack initiation position in experiments is located around the flaw center, the crack can be determined as mode I crack. In contrast, the

crack initiation position of 90° sample has narrow extent ($\beta = 0^\circ$ and 180° or so), the crack can be determined as mode I crack if the crack initiation position in experiments is located around flaw tips. Therefore, samples with 0° and 90° inclination angles in experiments are selected to confirm the validity of this novel method.

3.2.1 Crack Initiation Mechanisms in 0° Sample

From the experimental results of 0° sample, two cracks initiated from the center of pre-existing flaw (Fig. 6a) and the corresponding initiation positions met the condition that the maximum tensile tangential stress is located in the zone ($\beta = 15^\circ - 165^\circ$). Based on the DIC calculation results and above determination method, the relative displacement components of deformational points between cracks can be obtained (Fig. 6b). As presented in Fig. 6c, d, the normal and shear relative displacements both have no obvious changes at the onset of axial loading, revealing the deformation of samples are continuous and no cracks initiate between these points. When the loading time reaches about 430 s for crack 1 and 500 s for crack 2 (point A), the normal relative displacement starts increasing while the shear relative displacement has no distinct variation yet, which suggests that the

Fig. 6 Relative displacement components of cracks initiated in sample with 0° pre-existing flaw during uniaxial compression; **a** schematic of cracks initiated from pre-existing flaw; **b** full-field displacement components in global coordinate when cracks initiate; **c** relative displacement components of crack 1 as a function of loading time; **d** relative displacement components of crack 2 with regard to loading time



cracks initiated in this moment are mainly caused by opening deformation along crack normal direction, the cracks can be determined as mode I cracks based on the formula (9). In addition, an interesting phenomenon is observed from the relative displacement curves. With the increase of loading time, the normal relative displacement first increases and then decreases (i.e., the grey areas in Fig. 6c, d). By analyzing the DIC results and the fracture processes, the initiation of cracks from flaw tips may lead to the closure of the cracks initiated from flaw center, resulting in the decrease of the normal relative displacement (Liu et al. 2020).

3.2.2 Crack Initiation Mechanisms in 90° Sample

Figure 7 shows the relative displacements of deformational points in 90° sample. Similarly, two cracks initiated from the flaw tips (Fig. 7a, b) and their initiation positions are located in the zone where maximum tensile tangential stress concentrates ($\beta=0^\circ$ and 180° or so). From the DIC results of cracks 1 and 2 (Fig. 7c, d), the normal and shear relative displacements have no pronounced variations at the onset of loading. As the loading time increases to 1500 s or so, the normal relative displacement starts increasing significantly, while the shear relative displacement has no pronounced

changes. Therefore, these cracks are mainly initiated by the opening deformation along crack normal direction, illustrating these cracks are mode I cracks.

From the above analysis, the novel method proposed in this study is confirmed to be valid and it is reliable to determine crack initiation mechanisms in other pre-cracked samples.

4 Experimental Results

4.1 Crack Types with Different Initiation Mechanisms in Pre-cracked Samples

By utilizing the novel method, three types of cracks with different initiation mechanisms have been determined in samples containing a single pre-existing flaw with different inclination angles. In addition to the mode I cracks found in 0° and 90° samples, the mode II crack and mixed mode I/II crack were identified in other pre-cracked samples. When the mixed mode I/II cracks initiate, the normal and shear relative displacements occur at the same time, indicating that the opening deformation along crack normal direction and the sliding deformation along crack shear

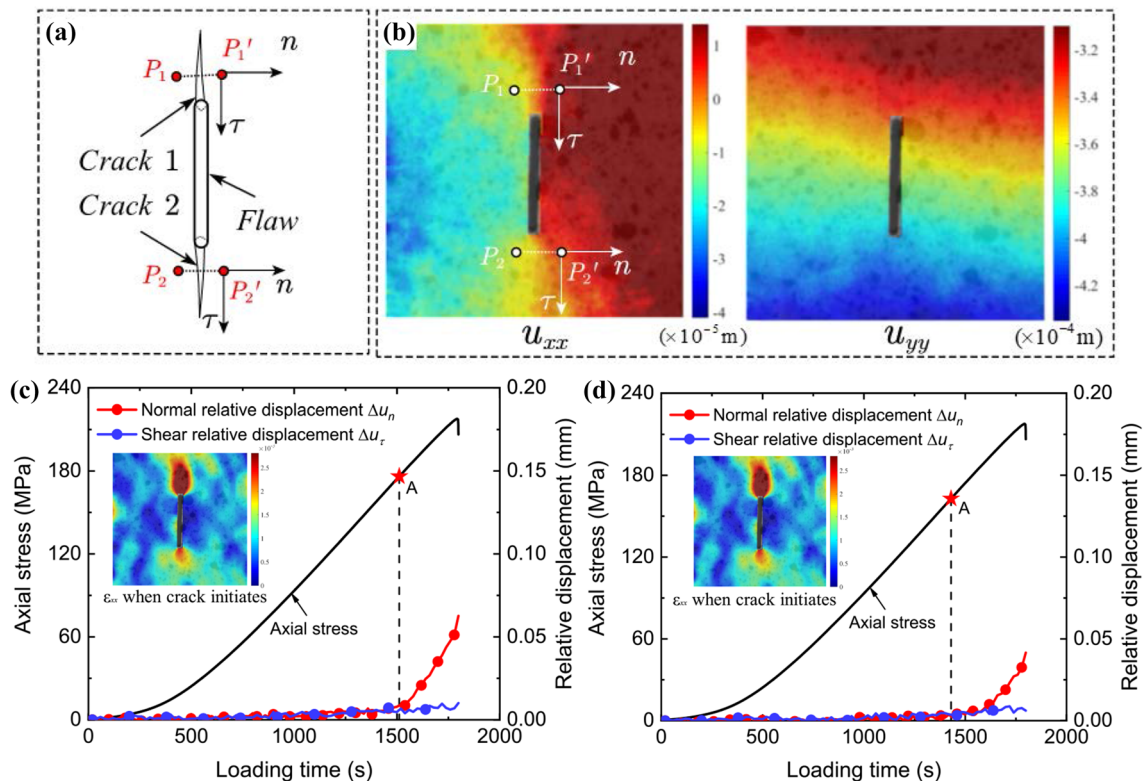


Fig. 7 Relative displacements of cracks initiated in sample with 90° pre-existing flaw during uniaxial compression; **a** schematic of cracks initiated from pre-existing flaw; **b** displacement fields in global coordinates; **c** variation of relative displacements of crack 1 as a function of loading time; **d** variation of relative displacements of crack 2 with respect to loading time

direction exist simultaneously. Here, taking the 30° sample for instance, four cracks were initiated from pre-existing flaw tips when the sample was loaded to failure (Fig. 8a, b). To elucidate the processes for determining initiation mechanisms of mixed mode I/II cracks and mode II cracks, the cracks 1 and 3 are selected for following analysis.

4.2 Mixed Mode I/II Cracks

When the crack 3 initiates, the strain and displacement contours (u_{xx} and ϵ_{xx}) calculated by DIC analysis are shown in Fig. 8c, the variation of relative displacements as a function of loading time is presented in Fig. 8e. Different to mode I cracks, when the axial loading time reaches 700 s or so (point A), the normal relative displacement as well as the shear relative displacement of crack 3 begins increasing at nearly the same time, suggesting that the opening deformation along crack normal direction and sliding deformation along crack shear direction appear simultaneously, the crack is identified as mixed mode I/II crack. When the loading

time reaches about 1100 s, the normal and shear relative displacements begin to decrease, which may be induced by the initiation of crack 1.

4.3 Mode II Cracks

Figure 8d presents the strain and displacement contours (u_{xx} and ϵ_{xx}) of the crack 1, and the variation of relative displacements as a function of loading time is shown in Fig. 8f. When the loading time reaches about 700 s (point A), the shear relative displacement starts increasing, while the normal relative displacement has no pronounced changes until the loading time reaches about 1000 s (point B). The increase of shear relative displacement prior to the normal relative displacement indicates that the sliding deformation along crack shear direction is the dominant driven factor for crack initiation, the crack is, therefore, defined as mode II crack.

Apart from above variation trend of relative displacements for determining mode II cracks, another

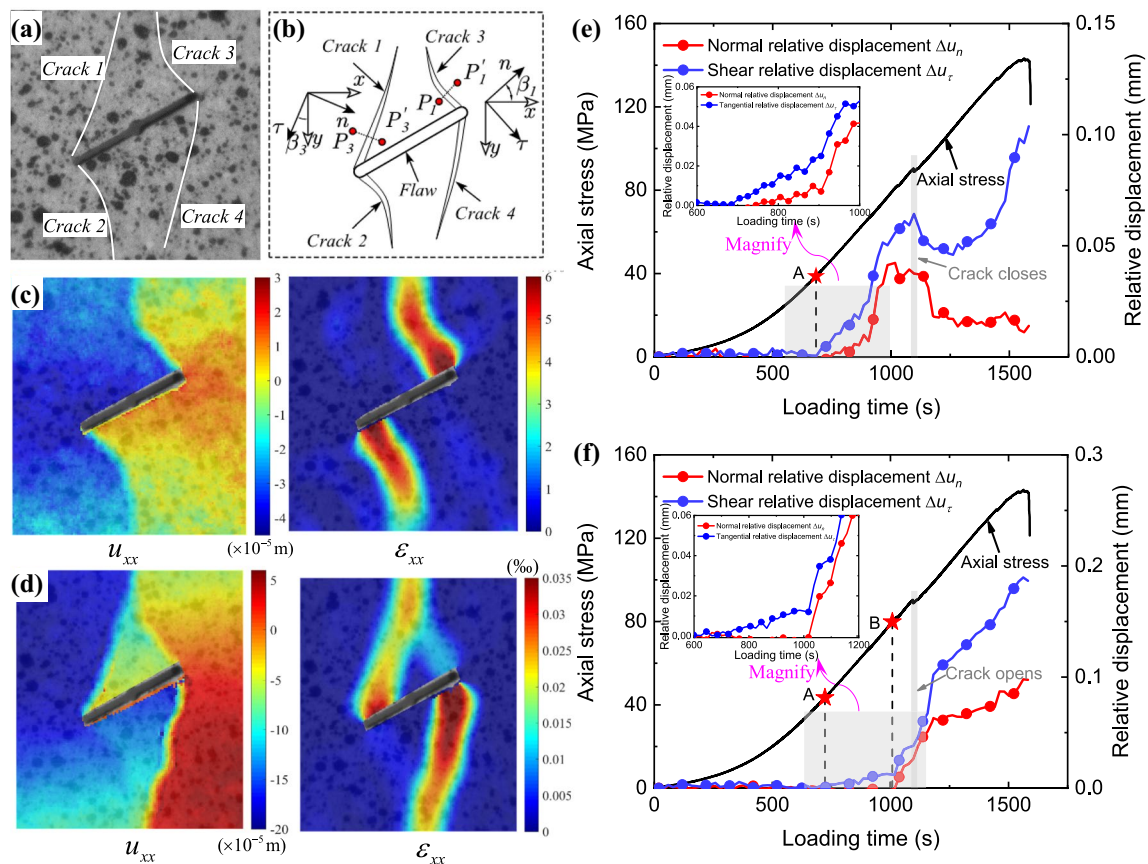


Fig. 8 The types of cracks initiated in samples with 30° pre-existing flaw; **a** cracks initiated from flaw when sample fails; **b** calculation schematic of cracks 1 and 3; **c**, **d** displacement and strain (u_{xx} and ϵ_{xx}) distributions when cracks 1 and 3 generate from flaw tips; **e** relative

displacements of points between crack 3 with regard to loading time; **f** relative displacements of points between crack 1 as a function of loading time

displacement variation tendency could be used to determine mode II cracks. As illustrated in Fig. 9a, the normal and shear relative displacements of the crack 1 in 60° sample begin changing once the uniaxial loading is applied. In addition, the normal relative displacement is negative and the shear relative displacement is positive. According to the formula (10) in Sect. 3.1, the negative relative displacement along crack normal direction would keep the crack surfaces touching during the whole loading and the sliding deformation along crack shear direction would induce the crack initiation (Fig. 9c). When the loading time increases to 1350 s or so, the shear relative displacement increases significantly and the strain localization phenomenon occurs around the flaw tips, indicating the crack is generated.

4.4 Crack Initiation Mechanisms Determined in Samples with Different Inclination Angles

According to the initiation characteristics of above three crack types, the crack initiation mechanisms in samples with different inclination angles were investigated. In this section, the cracks emanating in 45°, 60° and 75° samples are analyzed in detail.

4.4.1 Crack Initiation Mechanisms in 45° Sample

Figure 10 illustrates the relative displacements of cracks in 45° sample, four cracks were initiated from flaw tips. For crack 3 (Fig. 10c), when the axial loading time reaches around point A, the normal and shear relative displacements increase at the nearly same time, suggesting the opening deformation along crack normal direction and the sliding

deformation along crack shear direction occur simultaneously. Thus, the crack can be determined as mixed mode I/II crack. As for crack 2 (Fig. 10b), the normal relative displacement increases at the loading time point A, while the shear relative displacement has no obvious changes. Therefore, the opening deformation along crack normal direction is the predominant underlying mechanism for crack initiation, the crack is identified as mode I crack. Regarding cracks 1 and 4 (Fig. 10a, d), the shear relative displacement increases before the increase of normal relative displacement, which presents that the crack initiation is induced by sliding deformation along crack shear direction, the cracks are determined as mode II cracks. Furthermore, the formation processes of macroscopic cracks 1 and 4 are violent and accompanied with the simultaneous and considerable increase of normal and shear relative displacements (grey areas in Fig. 10a, d). Therefore, it is difficult to utilize high-speed camera to accurately identify crack initiation mechanisms using naked eyes to observe the occurrence of macroscopic cracks.

4.4.2 Crack Initiation Mechanisms in 60° Sample

Figure 11 shows the relative displacements of cracks initiated from flaw tips in 60° sample. In addition to the crack 1 which has been identified as mode II crack in Sect. 4.1.2, cracks 2, 3 and 4 were initiated during the experiments. As for cracks 2 and 3 (Fig. 11a, c), the relative displacements along crack normal and shear directions simultaneously increase at the loading time point A, indicating that the opening deformation along crack normal direction and sliding deformation along crack shear direction are the underlying mechanism for crack initiation, these cracks are consequently identified as mixed mode I/II cracks. In terms of

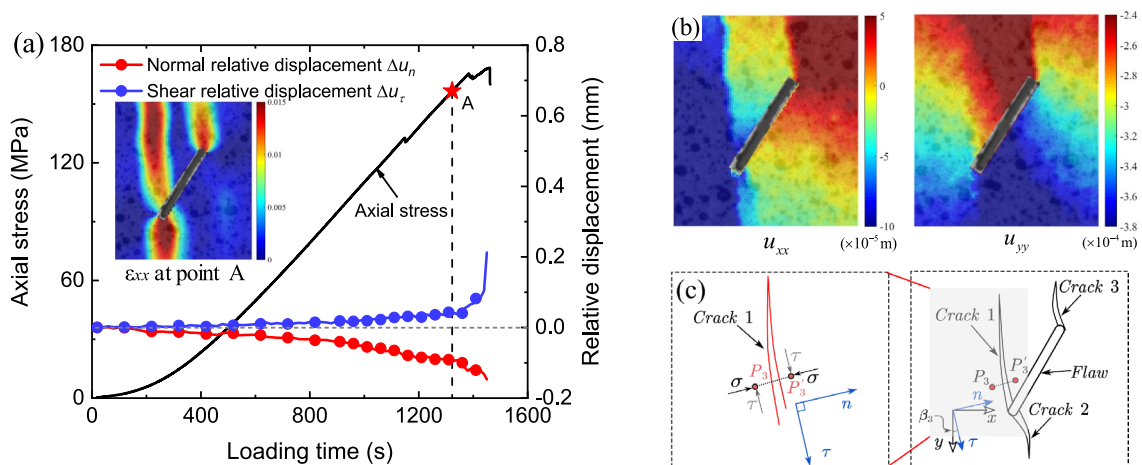


Fig. 9 Another variation trend of relative displacement for determining mode II cracks initiated in pre-cracked samples; **a** relative displacements of monitoring points in 60° sample with regard to load-

ing time; **b** global displacement distributions around flaw when the loading time reaches point A; **c** schematic for determining initiation mechanism of crack 1

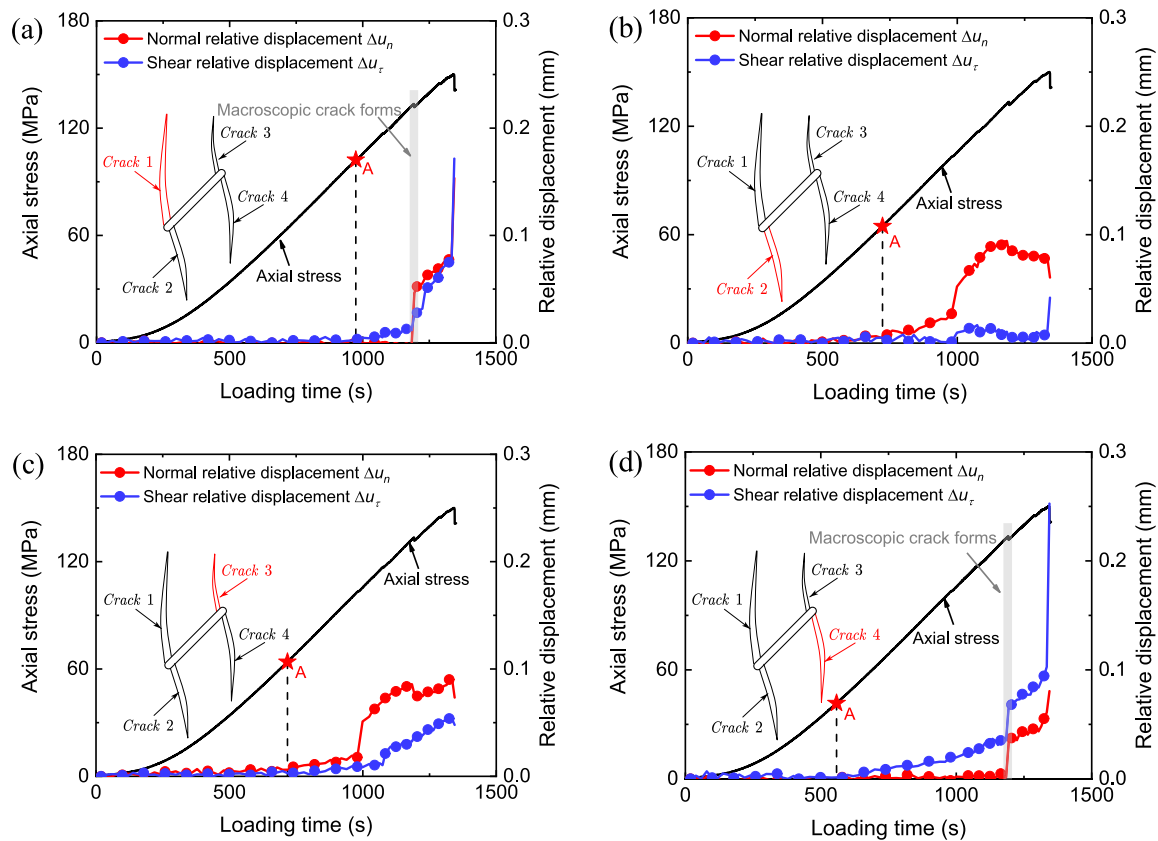


Fig. 10 Determination on initiation mechanisms of cracks emanating from flaw tips in 45° sample; **a** relative displacement of crack 1 with regard to loading time; **b** relative displacement of crack 2 with

respect to loading time; **c** relative displacement of crack 3 with regard to loading time; **d** relative displacement of crack 4 with respect to loading time

crack 4, the normal relative displacement begins increasing at the point A, while the shear relative displacement does not change until the suddenly formed macroscopic crack appears (grey area in Fig. 11d). Therefore, the crack is induced by sliding deformation along shear direction and determined as mode II crack. Likewise, when the macroscopic cracks 1 and 4 generate from flaw tips, the normal and shear relative displacements increase in the same time.

4.4.3 Crack Initiation Mechanisms in 75° Sample

Figure 12 reveals the relative displacements of cracks initiated from flaw tips in 75° sample. Similar to 90° sample, two cracks were initiated from flaw tips. When the loading time reaches around point A, the normal relative displacements of two cracks increase significantly. The shear relative displacement of crack 1 has no evident changes, while the shear relative displacement of crack 2 increases slightly, thus the crack 1 is determined as mode I crack and the crack 2 is determined as mixed mode I/II crack.

4.5 The Effect of Inclination Angle on Crack Initiation Mechanisms

Table 1 displays the crack initiation mechanisms in samples containing a single flaw with different inclination angles, three types of cracks with different initiation mechanisms were found in these samples. According to the crack classification of Wong and Einstein (2009a, b), Bobet and Einstein (1998), Park and Bobet (2009), Bobet (2000), and Yang and Jing (2011), these cracks can be classified into two types, namely wing cracks and anti-wing cracks. Based on the initiation mechanisms, the wing cracks consist of mixed mode I/II cracks and mode I cracks, while the anti-wing cracks are mainly mode II cracks (Table 1). When the inclination angle is less than 75°, the wing cracks and anti-wing cracks both emanate from pre-existing flaw. The wing cracks are mainly mixed mode I/II cracks, and the anti-wing cracks are mainly mode II cracks. Using high-speed camera, Wong and Einstein (2009b) obtained the similar results that the mixed tensile-shear cracks (i.e., mixed mode I/II cracks in

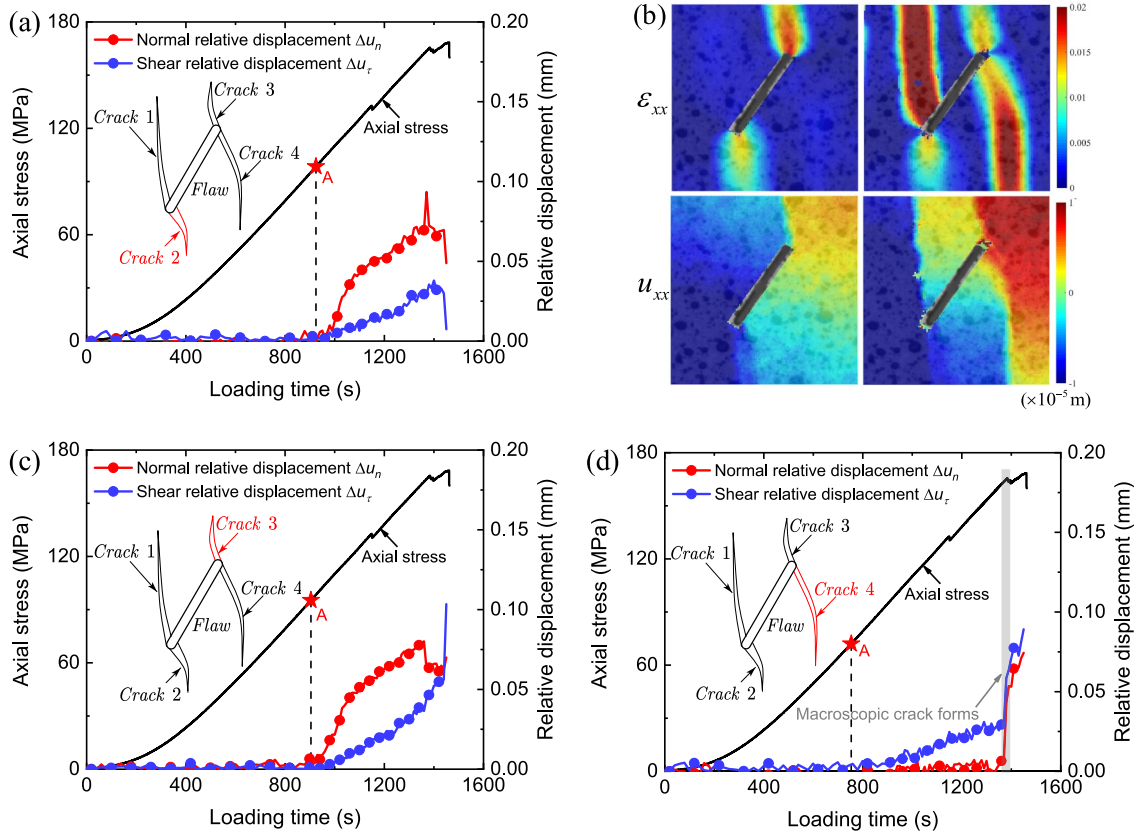


Fig. 11 Determination on initiation mechanisms of cracks emanating from flaw tips in 60° sample; **a** relative displacement of crack 2 as a function of loading time; **b** strain and displacement distributions

when cracks initiate; **c** relative displacement of crack 3 as a function of loading time; **d** relative displacement of crack 4 as a function of loading time

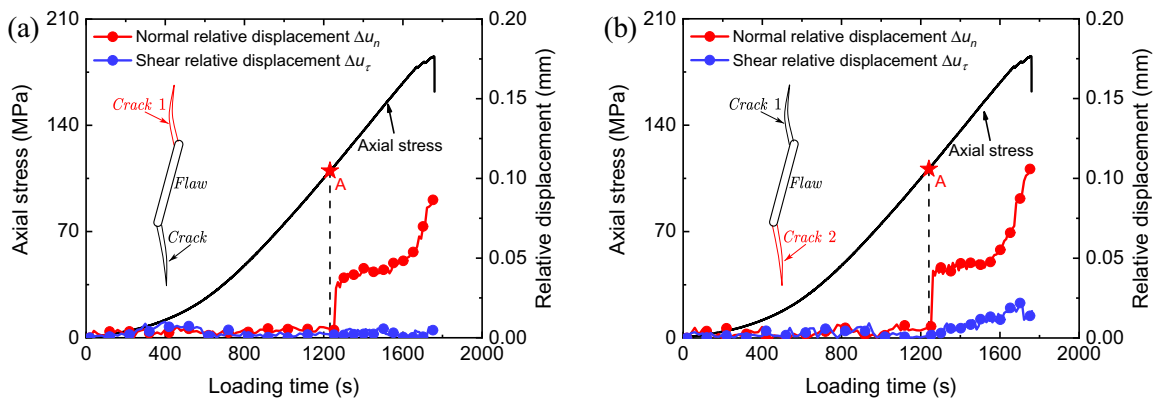


Fig. 12 Determination on initiation mechanisms of cracks initiated from flaw tips in 75° sample; **a** relative displacement of crack 1 with regard to loading time; **b** relative displacement of crack 2 with regard to loading time

this study) are common in samples with small and medium inclination angles. In addition, Maji et al. (1991) concluded that the wing cracks initiated from flaws were tensile-shear cracks by utilizing holographic interferometry technique for experiments. In contrast, the total number of cracks initiated

in 75° and 90° samples is less and the wing cracks initiated from flaw tips are mainly mode I cracks. With the increase of inclination angles, the wing cracks generally changes from mixed mode I/II cracks to mode I cracks, while the anti-wing cracks are commonly mode II cracks.

5 Discussion

To interpret the crack initiation mechanisms determined in experiments and to provide the reason why crack initiation mechanisms change with respect to inclination angles, the full-field tangential stress around elliptical cracks under uniaxial compression has been analyzed based on the theoretical derivation of Wu and Chang (1978) and Maugis (1992) as follows:

$$\frac{\sigma_{\beta\beta}}{\sigma_0} = \frac{1}{2}[B + \lambda(A \sinh 2\xi - C \sin 2\beta - [\cosh 2(\xi - \xi_0) - 1](B \cos 2\beta + C \sin 2\beta) + (\cosh 2\xi_0 - \cos 2\beta)[B + \lambda(A \sinh 2\xi - C \sin 2\beta)])], \tag{12}$$

$$\lambda = \frac{1}{\cosh 2\xi - \cos 2\beta}, \quad A = 1 - e^{2\xi_0} \cos 2\left(\frac{\pi}{2} - \theta\right), \tag{13}$$

$$B = e^{2\xi_0} \cos 2\left(\frac{\pi}{2} - \theta\right), \quad C = e^{2\xi_0} \sin 2\left(\frac{\pi}{2} - \theta\right)$$

where $\sigma_{\beta\beta}$ is the tangential stress around elliptical cracks, σ_0 is the applied compressive stress, ξ is a parameter in elliptical coordinate, ξ_0 represents the crack boundary, β is the angle of points on the crack boundary with respect to the direction of crack long axis, and θ is the inclination angle of crack long axis in this study (Fig. 5a).

Figure 13b–h show the theoretical full-field tangential stress in samples with different inclination angles θ . The tensile and compressive tangential stress are distributed

around elliptical cracks and samples with different inclination angles have various stress distributions. In the case of 0° sample, tensile tangential stress is located in the central zones of flaw and the compressive tangential stress is located around the flaw tips. As the inclination angle θ becomes larger, the positions of tensile tangential stress zones shift from the flaw center to flaw tips and the compressive tangential stress shift from flaw tips to flaw center. When the inclination angle θ approaches 90° , the tangential stress around flaw tips become tensile stress and the tangential stress around the flaw center become compressive stress.

In terms of the zones where wing cracks initiate, the tangential stress is dominated by tensile stress. Since the tensile strength of rock material is lower than its compressive strength, the tensile tangential stress would result in the opening deformation along the normal direction of wing cracks. In contrast, the tangential stress among zones where anti-wing cracks initiate is dominated by compressive stress, which induces that the two sides of anti-wing cracks touch to each other. In addition, the upper and bottom surfaces of elliptical cracks could be regarded as simply supported beams. Under the axial compressive loading, the surfaces of elliptical crack deform to each other, inducing the occurrence of sliding deformation along crack shear directions of wing and anti-wing cracks (Fig. 13a). Therefore, the tensile tangential stress and the sliding deformation along crack shear direction would result in the initiation of wing cracks as mixed mode I/II cracks, the

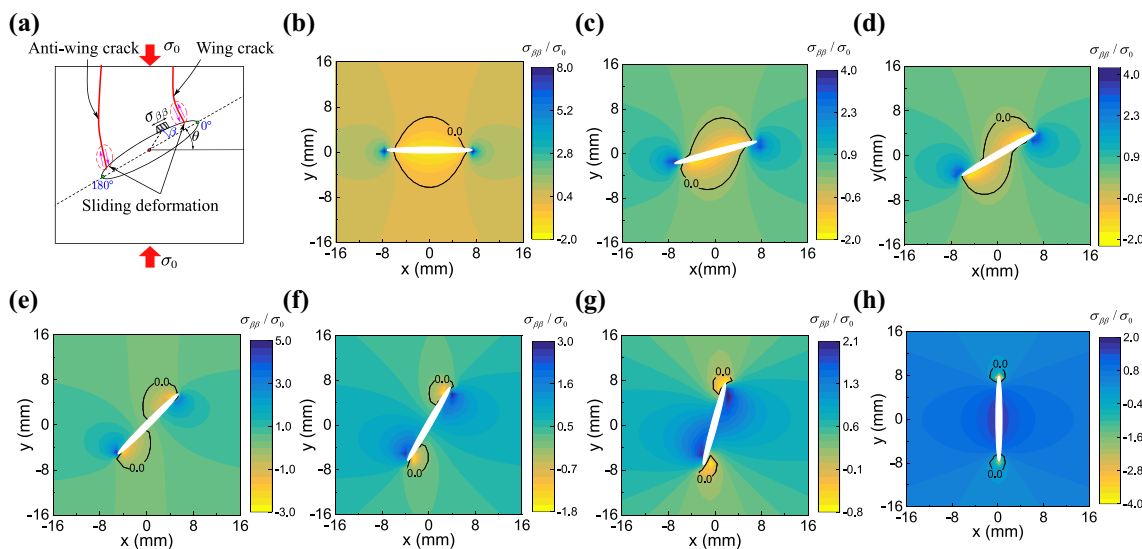
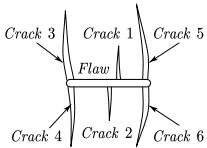
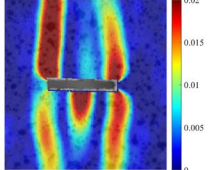
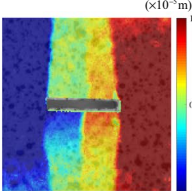
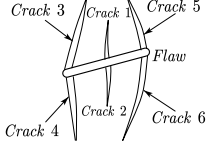
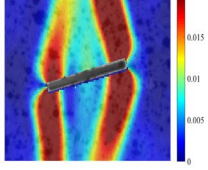
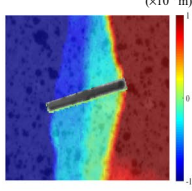
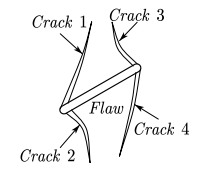
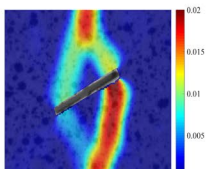
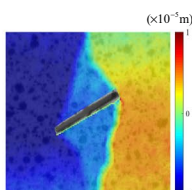
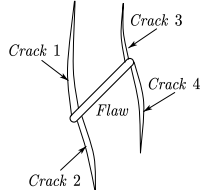
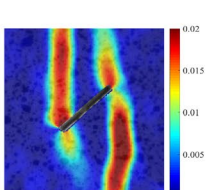
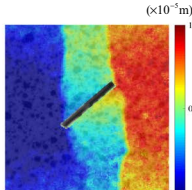
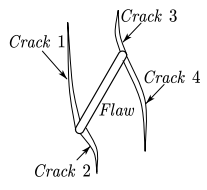
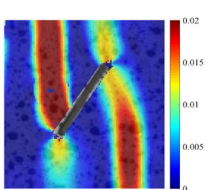
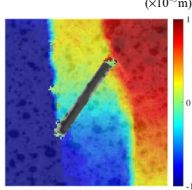
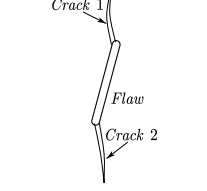
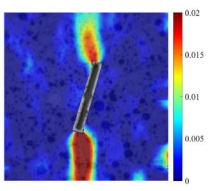
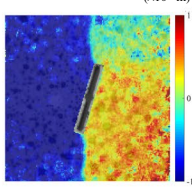
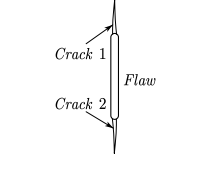
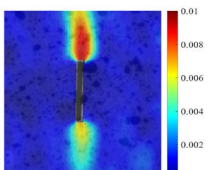
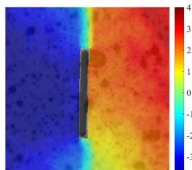


Fig. 13 Schematic of cracks initiated from pre-existing flaw and the theoretical full-field tangential stress of samples with different inclination angles; **a** schematic of wing crack and anti-wing crack initiated from pre-existing flaw; **b** theoretical full-field tangential stress of 0° sample; **c** theoretical full-field tangential stress of 15° sample; **d** theo-

retical full-field tangential stress of 30° sample; **e** theoretical full-field tangential stress of 45° sample; **f** theoretical full-field tangential stress of 60° sample; **g** theoretical full-field tangential stress of 75° sample; **h** theoretical full-field tangential stress of 90° sample

Table 1 Crack initiation mechanisms in samples containing a single flaw with different inclination angles

θ	Crack distribution	ε_{xx}	u_{xx} ($\times 10^{-5}$ m)	Comments
0°				Mode I cracks: crack 1 and crack 2 Mode II cracks: crack 3 and crack 5 Mixed mode I/II cracks: cracks 4 and 6
15°				Mode I cracks: crack 1 and crack 2 Mode II cracks: crack 3 and crack 6 Mixed mode I/II cracks: cracks 4 and 5
30°				Mode I cracks: no cracks Mode II cracks: crack 1 and crack 4 Mixed mode I/II cracks: cracks 2 and 3
45°				Mode I cracks: crack 2 Mode II cracks: crack 1 and crack 4 Mixed mode I/II cracks: crack 3
60°				Mode I cracks: no cracks Mode II cracks: crack 1 and crack 4 Mixed mode I/II cracks: cracks 2 and 3
75°				Mode I cracks: crack 1 Mode II cracks: no cracks Mixed mode I/II cracks: crack 2
90°				Mode I cracks: crack 1 and crack 2 Mode II cracks: no cracks Mixed mode I/II cracks: no cracks

For 0° sample, it is ambiguous to distinguish wing cracks and anti-wing cracks; for 15° sample, cracks 4 and 5 are defined as wing cracks, cracks 3 and 6 are defined as anti-wing cracks; for 30°–60° samples, cracks 1 and 4 are defined as anti-wing cracks, cracks 2 and 3 are defined as wing cracks; for 75°–90° samples, cracks 1 and 2 are defined as wing cracks

compressive tangential stress and the sliding deformation would induce the initiation of anti-wing cracks as mode II cracks. As for mode I cracks determined in 75° and 90°

samples, the sliding deformation along the shear direction of wing cracks is constrained due to the decrease of the length of simply supported beams, the opening deformation

induced by tensile tangential stress is the main driven factor for the crack initiation. Therefore, the initiation mechanisms of wing cracks alter from mixed mode I/II cracks to mode I cracks with the increase of inclination angles.

6 Conclusions

In this study, the crack initiation mechanisms in samples containing a single pre-existing flaw were quantitatively determined by using a novel method that was proposed based on DIC analysis. In light of the theoretical solution of full-field tangential stress distributed around pre-existing flaw and the deformation characteristics of flaw upper and bottom surfaces, the interpretation for the variation of crack initiation mechanisms with respect to inclination angles was provided, and the main conclusions are following:

1. In cooperation with digital image correlation analysis, a novel method that could quantitatively identify the crack initiation mechanisms was proposed and validated. Using this method, three types of cracks with different underlying initiation mechanisms have been found in samples containing a single pre-existing flaw, including mode I cracks, mode II cracks and mixed mode I/II cracks.
2. The initiation mechanisms of cracks emanating from different places around flaws (i.e., wing cracks and anti-wing cracks) are different and influenced by inclination angles. When the inclination angle is small, the wing cracks are predominated by mixed mode I/II cracks. As the inclination angle approaches 90°, the wing cracks change from mixed mode I/II cracks to mode I cracks. Comparatively, the inclination angle has little impact on the initiation mechanism of anti-wing cracks which are mainly mode II cracks in terms of different samples.
3. Based on the theoretical full-field tangential stress distribution, the tensile tangential stress occurred in the positions where wing cracks initiate leads to the opening deformation along crack normal direction. The compressive tangential stress occurred in the positions where anti-wing cracks emanate keeps the sliding surfaces of cracks touching during the entire initiation process. In the meanwhile, the upper and bottom surfaces of pre-existing flaw deform to each other, resulting in the occurrence of sliding deformation along crack shear direction. When the opening deformation exists and the sliding deformation is small, the wing cracks are mode I cracks. When the opening and sliding deformation appear simultaneously, the wing cracks are mixed mode I/II cracks. When the sliding surfaces of cracks keep in contact and the sliding deformation exists, the anti-wing cracks are mode II cracks.
4. Under compression, the upper and bottom surfaces of pre-existing flaw can be envisaged as simply supported beam. With the increase of inclination angles, the length of beam becomes smaller, inducing that the sliding deformation along crack shear direction is constrained. As a consequence, the wing cracks are prone to be mainly initiated by opening deformation, resulting in the change of initiation mechanisms from mixed mode I/II cracks to mode I cracks.

Even though three types of cracks generated with different initiation mechanisms have been found in samples containing a single pre-existing flaw by utilizing a quantitative method that was proposed and validated in this study, the propagation and coalescence mechanism of samples containing multiple pre-existing flaws is still ambiguous. Therefore, further studies should be conducted and the quantitative method proposed based on digital image correlation analysis might be helpful.

Acknowledgements This work is supported by the National Natural Science Foundation of China (Nos. 51439008, 51809137 and 41525009) and the Natural Science Foundation of Jiangsu Province (BK 20180480). The authors would like to thank the anonymous reviews and editors for their constructive suggestions which greatly improve the quality of this manuscript. The first author would like to thank Dr. Jun Zhou from Wuhan Institute of Rock and Soil Mechanics for his assistance in the experiments.

Compliance With Ethical Standards

Conflict of Interest The authors have declared that we have no financial and personal relationships with other people or organizations that can inappropriately influence our work.

References

- Bieniawski ZT (1967a) Mechanism of brittle fracture of rock. Part II-experimental studies. *Int J Rock Mech Min Sci* 4:407–423. [https://doi.org/10.1016/0148-9062\(67\)90031-9](https://doi.org/10.1016/0148-9062(67)90031-9)
- Bieniawski ZT (1967b) Mechanism of brittle fracture of rock. Part I-theory of the fracture process. *Int J Rock Mech Min Sci* 4:395–406. [https://doi.org/10.1016/0148-9062\(67\)90030-7](https://doi.org/10.1016/0148-9062(67)90030-7)
- Blaber J, Adair B, Antoniou A (2015) Ncorr: open-source 2D digital image correlation matlab software. *Exp Mech* 55:1105–1122. <https://doi.org/10.1007/s11340-015-0009-1>
- Bobet A (2000) The initiation of secondary cracks in compression. *Eng Fract Mech* 66:187–219. [https://doi.org/10.1016/S0013-7944\(00\)00009-6](https://doi.org/10.1016/S0013-7944(00)00009-6)
- Bobet A, Einstein HH (1998) Fracture coalescence in rock-type materials under uniaxial and biaxial compression. *Int J Rock Mech Min Sci* 35:863–888. [https://doi.org/10.1016/S0148-9062\(98\)00005-9](https://doi.org/10.1016/S0148-9062(98)00005-9)
- Bombolakis EG (1968) Photoelastic study of initial stages of brittle fracture in compression. *Tectonophysics* 6:461–473. [https://doi.org/10.1016/0040-1951\(68\)90072-3](https://doi.org/10.1016/0040-1951(68)90072-3)
- Brideau MA, Yan M, Stead D (2009) The role of tectonic damage and brittle rock fracture in the development of large rock slope

- failures. *Geomorphology* 103:30–49. <https://doi.org/10.1016/j.geomorph.2008.04.010>
- Chu TC, Ranson WF, Sutton MA (1985) Applications of digital-image-correlation techniques to experimental mechanics. *Exp Mech* 25:232–244. <https://doi.org/10.1007/BF02325092>
- Eberhardt E, Stead D, Stimpson B, Read RS (1998) Identifying crack initiation and propagation thresholds in brittle rock. *Can Geotech J* 35:222–233. <https://doi.org/10.1139/t97-091>
- Esterhuizen GS, Dolinar DR, Ellenberger JL (2011) Pillar strength in underground stone mines in the United States. *Int J Rock Mech Min Sci* 48:42–50. <https://doi.org/10.1016/j.ijrmms.2010.06.003>
- Guy N, Seyed DM, Hild F (2018) Characterizing fracturing of clay-rich lower watrous rock: from laboratory experiments to nonlocal damage-based simulations. *Rock Mech Rock Eng* 51:1777–1787. <https://doi.org/10.1007/s00603-018-1432-2>
- Horii H, Nemat-Nasser S (1985) Compression-induced microcrack growth in brittle solids: axial splitting and shear failure. *J Geophys Res* 90:3105. <https://doi.org/10.1029/jb090ib04p03105>
- Irwin GR (1957) Analysis of stresses and strains near the end of a crack traversing a plate. *J Appl Mech* 24:361–364
- Ju M, Li J, Li X, Zhao J (2019a) Fracture surface morphology of brittle geomaterials influenced by loading rate and grain size. *Int J Impact Eng* 133:103363. <https://doi.org/10.1016/j.ijimpeng.2019.103363>
- Ju M, Li J, Yao Q et al (2019b) Rate effect on crack propagation measurement results with crack propagation gauge, digital image correlation, and visual methods. *Eng Fract Mech* 219:106537. <https://doi.org/10.1016/j.engfracmech.2019.106537>
- Lajtai EZ (1971) A theoretical and experimental evaluation of the Griffith theory of brittle fracture. *Tectonophysics* 11:129–156. [https://doi.org/10.1016/0040-1951\(71\)90060-6](https://doi.org/10.1016/0040-1951(71)90060-6)
- Lee H, Jeon S (2011) An experimental and numerical study of fracture coalescence in pre-cracked specimens under uniaxial compression. *Int J Solids Struct* 48:979–999. <https://doi.org/10.1016/j.ijsolstr.2010.12.001>
- Li YP, Chen LZ, Wang YH (2005) Experimental research on pre-cracked marble under compression. *Int J Solids Struct* 42:2505–2516. <https://doi.org/10.1016/j.ijsolstr.2004.09.033>
- Li XF, Li HB, Zhang QB, Zhao J (2018a) Dynamic tensile behaviours of heterogeneous rocks: the grain scale fracturing characteristics on strength and fragmentation. *Int J Impact Eng* 118:98–118. <https://doi.org/10.1016/j.ijimpeng.2018.04.006>
- Li XF, Zhang QB, Li HB, Zhao J (2018b) Grain-Based Discrete Element Method (GB-DEM) modelling of multi-scale fracturing in rocks under dynamic loading. *Rock Mech Rock Eng* 51:3785–3817. <https://doi.org/10.1007/s00603-018-1566-2>
- Li XF, Li HB, Zhao J (2019) The role of transgranular capability in grain-based modelling of crystalline rocks. *Comput Geotech* 110:161–183. <https://doi.org/10.1016/j.compgeo.2019.02.018>
- Li XF, Li HB, Liu LW et al (2020) Investigating the crack initiation and propagation mechanism in brittle rocks using grain-based finite-discrete element method. *Int J Rock Mech Min Sci* 127:104219. <https://doi.org/10.1016/j.ijrmms.2020.104219>
- Liu L, Li H, Li X, Wu R (2020) Full-field strain evolution and characteristic stress levels of rocks containing a single pre-existing flaw under uniaxial compression. *Bull Eng Geol Environ*. <https://doi.org/10.1007/s10064-020-01764-4>
- Lockner DA, Byerlee JD, Kuksenko V et al (1991) Quasi-static fault growth and shear fracture energy in granite. *Nature* 350:39–42. <https://doi.org/10.1038/350039a0>
- Maji AK, Tasdemir MA, Shah SP et al (1991) Mixed mode crack propagation in quasi-brittle materials. *Eng Fract Mech* 38:129–145. [https://doi.org/10.1016/0013-7944\(91\)90077-E](https://doi.org/10.1016/0013-7944(91)90077-E)
- Martin CD, Chandler NA (1994) The progressive fracture of Lac du Bonnet granite. *Int J Rock Mech Min Sci* 31:643–659. [https://doi.org/10.1016/0148-9062\(94\)90005-1](https://doi.org/10.1016/0148-9062(94)90005-1)
- Maugis D (1992) Around cracks and elliptical cavities : exact solutions. *Eng Fract Mech* 43:217–255
- Nemat-Nasser S, Horii H, Nemat-Nasser S (1982) Compression-induced nonplanar crack extension with application to splitting, exfoliation, and rockburst. *J Geophys Res* 87:6805–6821. <https://doi.org/10.1029/JB087iB08p06805>
- Ohno K, Ohtsu M (2010) Crack classification in concrete based on acoustic emission. *Constr Build Mater* 24:2339–2346. <https://doi.org/10.1016/j.conbuildmat.2010.05.004>
- Ohtsu M (1991) Simplified moment tensor analysis and unified decomposition of acoustic emission source: application to in situ hydrofracturing test. *J Geophys Res* 96:6211–6221. <https://doi.org/10.1029/90JB02689>
- Ohtsu M (1995) Acoustic emission theory for moment tensor analysis. *Res Nondestruct Eval* 6:169–184. <https://doi.org/10.1007/BF01606380>
- Pan B, Qian K, Xie H, Asundi A (2009) Two-dimensional digital image correlation for in-plane displacement and strain measurement: a review. *Meas Sci Technol*. <https://doi.org/10.1088/0957-0233/20/6/062001>
- Pan B, Lu Z, Xie H (2010) Mean intensity gradient: An effective global parameter for quality assessment of the speckle patterns used in digital image correlation. *Opt Lasers Eng* 48:469–477. <https://doi.org/10.1016/j.optlaseng.2009.08.010>
- Park CH, Bobet A (2009) Crack coalescence in specimens with open and closed flaws: a comparison. *Int J Rock Mech Min Sci* 46:819–829. <https://doi.org/10.1016/j.ijrmms.2009.02.006>
- Petit J-P, Barquins M (1988) Can natural faults propagate under Mode II conditions? *Tectonics* 7:1243–1256. <https://doi.org/10.1029/TC007i006p01243>
- Reches Z, Lockner DA (1994) Nucleation and growth of faults in brittle rocks. *J Geophys Res*. <https://doi.org/10.1029/94jb00115>
- Rice JR (1980) Elastic wave emission from damage processes. *J Nondestruct Eval* 1:215–224. <https://doi.org/10.1007/BF00571803>
- Sagong M, Bobet A (2002) Coalescence of multiple flaws in a rock-model material in uniaxial compression. *Int J Rock Mech Min Sci* 39:229–241. [https://doi.org/10.1016/S1365-1609\(02\)00027-8](https://doi.org/10.1016/S1365-1609(02)00027-8)
- Scavia C (1995) A method for the study of crack propagation in rock structures. *Geotechnique* 45:447–463. <https://doi.org/10.1680/geot.1995.45.3.447>
- Shen B, Stephansson O, Einstein HH, Ghahreman B (1995) Coalescence of fractures under shear stresses in experiments. *J Geophys Res* 100:5975–5990. <https://doi.org/10.1029/95JB00040>
- Sibson RH (1985) Stopping of earthquake ruptures at dilatational jogs. *Nature* 316:248–251. <https://doi.org/10.1038/316248a0>
- Wong RHC, Chau KT (1998) Crack coalescence in a rock-like material containing two cracks. *Int J Rock Mech Min Sci* 35:147–164. [https://doi.org/10.1016/S0148-9062\(97\)00303-3](https://doi.org/10.1016/S0148-9062(97)00303-3)
- Wong LNY, Einstein H (2006) Fracturing behavior of prismatic specimens containing single flaws. In: *Proc 41st US Rock Mech Symp-ARMA's Golden Rocks 2006 - 50 Years Rock Mech*
- Wong LNY, Einstein HH (2009a) Crack coalescence in molded gypsum and carrara marble: part 1. Macroscopic observations and interpretation. *Rock Mech Rock Eng* 42:475–511. <https://doi.org/10.1007/s00603-008-0002-4>
- Wong LNY, Einstein HH (2009b) Systematic evaluation of cracking behavior in specimens containing single flaws under uniaxial compression. *Int J Rock Mech Min Sci* 46:239–249. <https://doi.org/10.1016/j.ijrmms.2008.03.006>
- Wong LNY, Xiong Q (2018) A method for multiscale interpretation of fracture processes in carrara marble specimen containing a single flaw under uniaxial compression. *J Geophys Res Solid Earth* 123:6459–6490. <https://doi.org/10.1029/2018JB015447>
- Wong RHC, Law CM, Chau KT, Shen ZW (2004) Crack propagation from 3-D surface fractures in PMMA and marble specimens under

- uniaxial compression. *Int J Rock Mech Min Sci* 41:1–6. <https://doi.org/10.1016/j.ijrmms.2004.03.016>
- Wu HC, Chang KJ (1978) Angled elliptic notch problem in compression and tension. *J Appl Mech Trans ASME* 45:258–262. <https://doi.org/10.1115/1.3424284>
- Xing HZ, Zhang QB, Braithwaite CH et al (2017) High-speed photography and digital optical measurement techniques for geomaterials: fundamentals and applications. *Rock Mech Rock Eng* 50:1611–1659. <https://doi.org/10.1007/s00603-016-1164-0>
- Yang SQ, Jing HW (2011) Strength failure and crack coalescence behavior of brittle sandstone samples containing a single fissure under uniaxial compression. *Int J Fract* 168:227–250. <https://doi.org/10.1007/s10704-010-9576-4>
- Yang SQ, Jiang YZ, Xu WY, Chen XQ (2008) Experimental investigation on strength and failure behavior of pre-cracked marble under conventional triaxial compression. *Int J Solids Struct* 45:4796–4819. <https://doi.org/10.1016/j.ijsolstr.2008.04.023>
- Yang SQ, Liu XR, Jing HW (2013) Experimental investigation on fracture coalescence behavior of red sandstone containing two unparallel fissures under uniaxial compression. *Int J Rock Mech Min Sci* 63:82–92. <https://doi.org/10.1016/j.ijrmms.2013.06.008>
- Yang SQ, Huang YH, Tian WL et al (2019) Effect of high temperature on deformation failure behavior of granite specimen containing a single fissure under uniaxial compression. *Rock Mech Rock Eng* 52:2087–2107. <https://doi.org/10.1007/s00603-018-1725-5>
- Zhang XP, Wong LNY (2012) Cracking processes in rock-like material containing a single flaw under uniaxial compression: a numerical study based on parallel bonded-particle model approach. *Rock Mech Rock Eng* 45:711–737. <https://doi.org/10.1007/s00603-011-0176-z>
- Zhao Y, Zhang L, Wang W et al (2016) Cracking and stress-strain behavior of rock-like material containing two flaws under uniaxial compression. *Rock Mech Rock Eng* 49:2665–2687. <https://doi.org/10.1007/s00603-016-0932-1>
- Zhao C, Meng ZY, Feng CZ, Bao C (2018) Cracking processes and coalescence modes in rock-like specimens with two parallel pre-existing cracks. *Rock Mech Rock Eng* 51:3377–3393. <https://doi.org/10.1007/s00603-018-1525-y>
- Zhao C, Niu J, Zhang Q et al (2019) Failure characteristics of rock-like materials with single flaws under uniaxial compression. *Bull Eng Geol Environ* 78:593–603. <https://doi.org/10.1007/s10064-018-1379-2>
- Zhou XP, Zhang JZ, Qian QH, Niu Y (2019) Experimental investigation of progressive cracking processes in granite under uniaxial loading using digital imaging and AE techniques. *J Struct Geol* 126:129–145. <https://doi.org/10.1016/j.jsg.2019.06.003>

Publisher's Note Springer Nature remains neutral with regard to jurisdictional claims in published maps and institutional affiliations.